Title

Atomic resolution phase contrast imaging and in-line electron holography using variable voltage and dose rate

Author

Bastian Barton

Publication Date

2012-10-14

Atomic resolution phase contrast imaging and in-line electron holography using variable voltage and dose rate

Brief title: *Low dose rate/voltage HRTEM*

Bastian Barton[1], Bin Jiang[2], ChengYu Song[3], Petra Specht[4], Hector Calderon[5] and Christian Kisielowski[3,6*]

[1]Materials Science Division, Lawrence Berkeley National Laboratory, 1 Cyclotron Road, Berkeley, CA 94720, USA

[2]FEI Company, 5350 NE Dawson Creek Drive, Hillsboro, OR 97124, USA

[3]National Center for Electron Microscopy, Lawrence Berkeley National Laboratory, 1 Cyclotron Road, Berkeley, CA 94720, USA

[4]Department of Materials Science and Engineering, University of California at Berkeley, Hearst Mining Bldg., Berkeley, CA 94720, USA

[5]Escuela Superior de Física y Matemáticas, IPN, Ed. 9 UPALM Zacatenco, Mexico D.F. 07738

[6]Joint Center for Artificial Photosynthesis, Lawrence Berkeley National Laboratory, 1 Cyclotron Road, Berkeley, CA 94720, USA

*Corresponding author. Phone +1 (510) 486-4716, fax +1 (510) 486-5888, email cfkisielowski@lbl.gov

Abstract

The TEAM 0.5 electron microscope is employed to demonstrate atomic resolution phase contrast imaging and focal series reconstruction with acceleration voltages between 20 and 300 kV and a variable dose rate. A monochromator with an energy spread of ≤0.1eV is used for dose variation by a factor of 1,000 and to provide a beam-limiting aperture. The sub-Ångstrøm performance of the instrument remains uncompromised. Using samples obtained from silicon wafers by chemical etching, the [200] atom dumbbell distance of 1.36 Å can be resolved in single images and reconstructed exit wave functions at 300, 80, and 50 kV. At 20 kV, atomic resolution < 2 Å is readily available but limited by residual lens aberrations at large scattering angles. Exit wave functions reconstructed from images recorded under low dose rate conditions show sharper atom peaks as compared to high dose rate. The observed dose rate dependence of the signal is explained by a reduction of beam-induced atom displacements. If a combined sample and instrument instability is considered, the experimental image contrast can be matched quantitatively to simulations. The described development allows for atomic resolution TEM of interfaces between soft and hard materials over a wide range of voltages and electron doses.

Keywords: In-line electron holography, aberration-corrected TEM, high resolution TEM, low voltage TEM, low dose TEM, monochromator, exit wave reconstruction, focal series, lattice phonons

Introduction

In recent years, significant progress has been made in transmission electron microscopy (TEM), driven by the development of aberration correctors (Haider et al., 1999; Kabius et al., 2009; Sawada et al., 2010) and other electron optical components such as monochromators and high brightness guns (Freitag et al., 2008; Tiemeijer et al., 2008, 2012). Leading-edge equipment allows now for single atom detection across the Periodic Table of Elements at an ultimate resolution limit around 0.5 Å, which is set by the Coulomb scattering process itself (Kisielowski et al., 2008, 2009; Alem et al., 2011). As the available brightness values now approach $3 \cdot 10^9$ A/cm^2/srad, the resulting beam current density reaches ~20 A/cm^2 or ~12,000 electrons/Å^{2}s when the emitted electrons are focused onto small areas. This high intensity can be expected to compromise the sample integrity even if radiation-hard crystalline materials are considered. Imaging of “soft” materials, characterized by low-atomic-number elements and relatively weak chemical bonds, becomes even less accessible. This is known from electron microscopy of native biological specimens, where the accumulated dose is typically limited to 10-20 e$^-$/Å^2 (Bammes et al., 2010).

Therefore, the accomplished performance improvements have drawn renewed attention to the significant beam-sample interactions that occur during the observation of electron transparent samples in advanced aberration-corrected TEMs (Specht et al., 2011a). Currently, strategies emerge to address this matter with low voltage microscopy (Kaiser et al., 2011), detector development (Battaglia et al, 2009) and dose minimization (Barton et al., 2011). Furthermore, it has become desirable to enable imaging of hard and soft matter composites, which are used in energy-related research efforts and are therefore of rapidly growing interest (www.solarfuelshub.org).

It is common practice for biologists and material scientists to work at medium acceleration voltages of 200 - 300 kV. This choice of voltage is rationalized in different ways: first, the ionization of hydrogen atoms as the dominant damage process decreases towards higher voltage (Kim & Rudd, 1994). Second, the penetration power of 300 kV electrons can exceed 500 nm, which allows for cellular tomography in some cases (Medalia et al., 2002). For materials scientists, a 200-300 kV microscope is preferred because it allows for atomic resolution even if lens aberrations are addressed only to second order (Erni 2010). The source brightness is essential, as the resolution increases with the square root of number of the detected electrons (Tiemeijer 2008). Nowadays, phase-contrast microscopy at low voltages between 20 and 80 kV becomes feasible, with the successful development of spherical and chromatic aberration (C_S, C_C) correctors that can correctly focus electrons scattered to high angles into an image point (Kisielowski et al., 2010a). At the same time, monochromators limit the energy spread to ≤100 meV and are stable during exposure times of typically 1s in the case of the TEAM 0.5.

Figure 1 describes the imaging conditions used in this work resulting from a high-brightness electron source, by plotting the utilized voltage-intensity parameter space. It is seen that decreasing the acceleration voltage from 300 kV to 20 kV decreases the beam power by about one order of magnitude. In contrast, a beam current variation at constant voltage allows us to change the power by more than three orders of magnitude. Both parameters are expected to affect beam-sample interactions in a different manner. It is established that the relative amount of displacement damage increases with increasing voltage, while the rate of ionization damage decreases and peaks at low energy (Egerton et al., 2004).

As the electron acceleration voltages decrease, challenges arise from increasing scattering angles and significantly shorter extinction oscillations. Furthermore, a defocus spread Δf of a few Å is needed to obtain atomic resolution, since the temporal damping

$E_D(k) = \exp(-½\, \pi^2 \lambda^2 \Delta^2 f\, k^4)$

for a spatial frequency k increases with the electron wavelength λ. A drop of the signal-to-noise-ratio (SNR) is unavoidable at low doses and must be compensated to produce image features above noise. These unsettled aspects can be addressed through new, adequate imaging conditions and detection schemes. However, these new techniques do not longer aim at recording a single image at a fixed focus value to show the recorded structure. Instead, we record large image series that are reconstructed to obtain the complex exit wave function with sufficient SNR.

In this paper, we report that atomic-resolution microscopy is achieved between 20 kV and 300 kV using the TEAM 0.5 microscope. A new illumination scheme uses the monochromator to reduce the beam current within the field of view to a small fraction of what is emitted from the high brightness source. The field of view is restricted to nearly match the square CCD detector, so that no other part of the sample is exposed to electrons. It is shown for Si [110] that atomic resolution can be obtained across the whole voltage range in single images recorded under high dose rate (HDR) conditions. Electron exit wave functions were reconstructed from focus series acquired under low dose rate (LDR) and HDR conditions. It is found that the method of iterative exit wave reconstruction (EWR) can be successfully applied to image series recorded at a dose rate of 12 $e^-/Å^2s$. As shown in Fig.1, this intensity is by a factor of ~1,000x lower than typically used in HRTEM with a high brightness source. The exit wave functions reconstructed from low dose rate images show an improved quality as compared to HDR conditions. Exit waves can be quantitatively matched to simulations if microscope and sample stabilities are considered.

Materials & Methods

The aberration-corrected TEAM 0.5 microscope was tuned to operate at 300, 80, 50 and 20 keV in four different experiments. Figure 2 shows the measured spherical aberration coefficients, relevant scattering angles, and the estimated resolution for the considered voltage range. 20 kV was chosen as the lowest voltage because the calculated displacement damage is negligible even for materials composed of light elements with small binding energies, such as diatomic molecules (Suppl. Fig. 1). A Wien filter-type monochromator is used for three purposes: First, the dispersed beam narrows the energy spread to ≤0.1 eV, which provides sufficient temporal coherence to reach sub-Å resolution. Second, as the beam intensity is distributed in a Gaussian shape along the energy-dispersive direction, the shift of an inserted slit in this direction allows for variation of the dose rate over several orders of magnitude. In this manner, we are able to reduce the current density from ~12,000 $e^-/Å^2s$ (HDR conditions) down to values as low as 12 $e^-/Å^2s$ (LDR conditions) at 80 kV. Switching between HDR and LDR conditions is possible in less than a second. Due to this shift, LDR imaging occurs with an energy difference of 5-10 eV compared to HDR. Third, the slit together with the dispersed beam serves as a square-shaped beam-limiting aperture that geometrically matches the field of view to the CCD detector (typically 24 x 24 nm^2 at 330,000 x primary magnification). A focal spread of the instrument of 7 Å was measured at 80 kV, which we assumed for all acceleration voltages. The convergence semi-angle under the described illumination conditions is ~0.1 mrad (Tiemeijer et al., 2008, 2012).

To produce Si[110] samples, we cut a wafer into 3 mm disks and prepared a plan view geometry by ion milling. This step was followed by chemical etching with potassium hydroxide (KOH) to produce the branch-like structure at the hole edge shown in Fig. 3. The native silicon oxide layer had been removed by hydrofluoric acid (HF) immediately before KOH etching. The etching process exposes {111} faces, so that the branches are rooftop-shaped in cross section. The wedges at the edge have angles of ~50° and are well-suited for HRTEM imaging.

Images were recorded on a 2048 x 2048 pixel CCD camera (Gatan, Pleasanton, USA), which was hardware-binned to 1024 pixels. Integration times varied between 0.5 and 1s. We acquired focal series containing up to 200 images across a focus range of ±25 nm. For low dose rate experiments, 5 images of each focus value were recorded and the aligned averages were used for focus series reconstruction.

EWRs were carried out using the software MacTempas (Total Resolution, Berkeley, USA), which uses a Gerchberg-Saxton algorithm for reconstruction as described by Hsieh et al. (2004). The software was modified to allow for processing of the large focal series. Spatial frequencies were retained within an aperture of 1.5 Å^{-1}. While a constant focus increment is used as a first guess, the software determines a refined focus value during the iterative process.

Multi-slice exit wave and imaging simulations of a Si[110] wedge were also performed using MacTempas. To compare with the experimental results, focal image series were calculated from exit waves using the same conditions (number of images, increment, aberrations) as in the experiment. Also, the measured values for the focal spread and convergence semi-angle were used as described above. The series were then used for EWR, using the focus refinement routine as in the experimental data. To make the data comparable, experimental images were corrected for the CCD's modulation transfer function (MTF; O'Keefe et al., 2001). Absorption was not included in the simulation.

Results

Atomic resolution imaging between 20 and 300 keV

Figure 4 shows edges of the Si[110] rooftop sample imaged at 300, 80, 50 and 20 keV using conventional HDR imaging with 3,200 to 16,000 e$^-$/Å^{2}s. From focal series, we selected images at overfoci of 60 - 90 Å, where the contrast transfer function (CTF) displays the characteristic 1.36 Å dumbbells with negative contrast (Lentzen 2004). The focus values were determined from the known increment, assuming that the image closest to Gaussian focus shows minimal contrast for the amorphous silica layer. Periodograms, i.e. noise-reduced power spectra, show reciprocal lattice vectors to ~1/0.60 Å for 300-50 kV. The <400> dumbbells are resolved at 50, 80 and 300 keV. While the shape of the double peaks indicates some decrease in resolution from 300 down to 50 keV, it is evident that the corrector sufficiently compensates the increased scattering angles (Fig. 2) to achieve a resolution close to 1 Å even at 50 keV.

The situation changes at 20 keV. In this case, reciprocal lattice vectors can only be observed to ~1/1.0 Å, and image contrast delocalization can be observed at the crystal edge in the real space image of Figure 4d. Although the [400] structure factor at 1/1.36 Å is present in the image spectrum, the dumbbells cannot be resolved at this electron energy (Fig. 4 h,l). This result is expected, as the scattering angles at 20 kV are more than four times larger than at 300 kV, and the presence of residual, higher order aberrations leads to a mis-phasing of the corresponding structure factors. Therefore, we tested the information limit for 20 keV in a Young's Fringe experiment. As shown in Figure 5a, the information limit can be estimated around 1.8 Å, which is slightly better than what is expected from the scattering angles. This is explained by Cc calculations and measurements that find a voltage dependent Cc of the microscopes UT lens of 0.9 mm already at 80 kV and 2.1 mm at 300 kV (Müller 2012). On the other hand, an increasing contribution of non-linear image components at low voltages can lead to an overestimation of the information limit derived from

Young's Fringes. However, the value can serve as a good estimate and is consistent with calculations.

In Figure 5b, a 20 keV diffraction pattern obtained from a thin Si[110] wedge is shown. At this electron energy, the Si <400> structure factor corresponds to a Bragg angle of 63.2 mrad, in contrast to 14.5 mrad for 300 kV. It can be seen that the hexapole optics of the corrector acts as an effective aperture, which severely distorts and dampens the signal for scattering angles higher than <400>. This is also reflected in the measurement error of the 5th order spherical aberration coefficient, which is about one order of magnitude larger at 20 kV as compared to 300 keV (Fig. 2).

Precision and stability of focal series reconstruction

The quality of an exit wave reconstruction depends on the precise determination of focal planes. To obtain meaningful reconstructions with atomic resolution and high phase and amplitude sensitivity, a precision comparable with the depth of focus is needed, corresponding to a few Å in TEAM 0.5. We used stepped focal series as an input to the program MacTempas to test the focus measurement precision as well as the stability of the TEAM 0.5. The program iteratively assigns an optimum focus value to each image of the focal series during reconstruction. Obviously, a change of any lens aberration as well as electrical and mechanical instrument instabilities will affect the measured focus value, wherefore we consider the procedure a suitable test for system stability. The result for a series of 50 images is shown in Fig. 6. The defocus was kept constant across 5 images and then decreased stepwise by 11 Å in over-focused images after each set of five images. The integration time per image was

0.5 s, with 0.7 s intervals between images. In the reconstruction process, a linear decrease by 2.2 Å per image was input to the algorithm as an initial guess. It can be seen that the software recovers the input step function reliably within an extraordinary small "focus" drift (standard deviation) of only 2.1 Å. Therefore, it can safely be assumed that the focus drift of the TEAM 0.5 microscope is stable within 2 Å during a time period of a few minutes. This enables an accurate exit wave reconstruction in LDR conditions, where single images are noise-dominated and provide little or no feedback to the microscopist within minutes of data acquisition.

In-line holography between 20 and 300 keV by focal series reconstruction

We applied foal series reconstruction to Si[110] rooftop samples in a ~5x5 nm area at the crystal edge at 300, 80, 50 and 20 keV. First we used conventional high dose rate conditions for imaging. As a reference focus, we chose the plane containing the tip of the Si wedge, which was determined by choosing an image from each series in which the contrast for the amorphous silica layer was minimal. We then propagated the calculated exit waves to a focal plane where we observed maximal phase peaks for the thinnest atom columns (at the tip). At 80 and 300 kV, these focal planes were all within 10 Å of the reference plane, and within 25 Å for 20 and 50 kV. The results after numerical correction for residual wave aberration and detector MTF are shown in Fig. 7. As in the single lattice images, the 1.36 Å dumbbells are resolved in the amplitudes and phases of the reconstructed object exit wave from 300-50 keV. The wave reconstruction at 20 kV gives meaningful phases for the Si[110] lattice projection, with the 5.44 Å spacing along <100> direction. Dumbbells cannot be resolved at 20 kV due to the residual aberration effects described above.

Phase profiles along [100] direction, from the vacuum to the thicker parts of the crystal wedge, show a sinusoidal modulation. The baseline of this modulation, which corresponds to the mean phase change by the top and bottom silica layers, is not constant. The reason for this is the absence of low spatial frequencies <0.1 Å^{-1}, which are poorly transferred even at the maximal defoci of +350 Å included in the series. Therefore, the atom column phases were measured as the difference of a maximum from the nearest minimum. These peak-to-valley phases reach a maximum that is voltage-dependent. The largest phases of ~1.3 rad are measured for 80 keV. The modulation can be explained in terms of the 1S state model of channeling theory, where amplitude and phase of the exit wave function are described in an Argand plot and produce a channeling map (Van Aert et al., 2007). The complex exit wave amplitudes Ψ_{peak} of atom columns with a thickness t lie on the circle

$$\Psi_{peak} = 1 - 2\, c_{00}\, \psi_{00} \sin(\pi\, t/D_{00}) \times \exp(-i\pi\, t/D_{00} + i\pi/2). \qquad (1)$$

ψ_{00} is the amplitude of the 1S Eigenfunction, c_{00} an excitation coefficient and D_{00} the periodical thickness. In a wedge-shaped object, the sample thickness increases roughly proportional to the distance from the edge, so that the phase peak modulation occurs perpendicular to the edge. It can also be seen from the data of Figure 7 that the phase maximum is reached earlier at lower energies. This is expected, as the periodical thickness is proportional to $(1 + 2m_0c^2/eU)^{-1/2}$. Periodical thicknesses (extinction distances) calculated from multi-slice simulations are listed in Table 1. It can be seen from Figure 8 that if $|2\, c_{00}\, \psi_{00}| < 1$, the phase as a function of thickness cannot exceed $\pi/2$, as observed in our data.

The exit plane of a wedge-shaped sample is not perpendicular to the beam axis (cf. Fig. 3c). Strictly, the reconstructions shown represent the actual exit wave only of atom columns at the wedge tip, while for thicker regions the wave is back-projected to the middle plane. For the phase at 80 kV shown in Fig. 7f, the EW had to be projected by 16 Å in beam direction to fulfill the maximal phase criterion for a column at ~48 Å distance from the edge. However, this small focal change did not give rise to any significant change in the 1.0 rad peak-to-valley phase of the column. When assuming a perfect 50° wedge, the exit surface of this column should be ~22 Å below the middle plane. There, the peak-to-valley phase was measured to be 0.9 rad.

Comparison of experimental data with multi-slice simulations

We performed multi-slice simulations for the TEAM 0.5 at 80 keV on a perfect Si [110] wedge, and compared the results to our data.Non-linear image contributions were neglected for simplicity. For thin parts of the wedge within ~5 nm from the tip, no significant differences in exit waves and images were found between calculations with and without non-linear components (data not shown). Model and results are shown in Figure 9. For the given sample geometry, the simulation predicts phase wrapping to occur at distance of ~ 8 nm from the edge, where 50% of the periodical thickness is reached (Fig. 9 b). The phases are faithfully reconstructed from a focal series of 40 images (Fig. 9d) except for spatial frequencies < 1 nm^{-1} that are not transferred by the CTF within the applied focus range. A Debye-Waller factor of 0.5

Å^2 is used. The situation changes drastically if additional atomic vibrations are considered. These may originate from the microscope or the sample and give rise to an additional damping in Fourier space of the form $\exp[-2(\pi\,\Delta x\,k)^2]$, where Δx is the standard deviation from the atomic lattice positions. For a displacement of 31 pm, the condition $|2\,c_{00}\,\psi_{00}| > 1$ is still fulfilled and the phase increases monotonically to π before wrapping (Fig. 8). However, displacements of ≥ 45 pm lead to a condition as shown in Fig. 8b. The phase does not reach π, instead it increases to a maximum of ~0.9-1.2 rad, followed by a decrease towards zero at $D_{00}/2$ (Fig. 9e). Dumbbell resolution is nearly lost for a vibration of 59 pm (Fig. 10b).

Exit wave reconstruction using low dose rates

Next, we performed focal series reconstructions of image series from the Si[110] rooftops at low dose rates, using 80 keV energy. An average of 12 e^-/Å^2, or 6 counts per CCD pixel over the field of view, was the lowest possible dose per image that still allowed sub-pixel alignment of the series. The beam intensity is thereby 1,000 times lower than under conventional HDR conditions. Images were recorded at 40 different focal planes with 1 s integration time, as described in the experimental section. Due to the chromatic aberration of 0.9 mm at 80 kV and the fact that the electron energy is lower by 5-10 eV in LDR conditions than in HDR, there will be a focus offset by ~60-120 nm between these two states. This effect was corrected by wave propagation. The results are shown in Fig. 11. While the SNR of individual images is low, each Fourier transform contains object structure factors with sub-atomic information transfer. The SNR of the aligned averages is sufficient to allow focal series alignment and reconstruction (see Materials & Methods). While the lattice structure can hardly be seen in single raw images, the EW modulus and phase clearly reveal the object. Even at this low dose rate and a total dose per series of ~4,100 $e^-/Å^2$, the 1.36 Å dumbbells are resolved. However, a maximum phase value of only 0.7 rad is measured, which is lower than for the HDR reconstruction from the same object area shown in Fig. 7. Signal loss due to imperfect image alignment and focus determination of noisy, individual images contribute to this effect.

Therefore, we compared a HDR exit wave reconstruction using 12,000 $e^-/Å^2$ to a LDR reconstruction recorded with a dose rate of 56 $e^-/Å^2$ (Fig. 12 a,b). A slightly higher dose rate than described above for LDR conditions was chosen to reduce alignment errors and allow direct comparison of the resolution. 2D Gaussian dumbbells were fitted to the exit wave phase within a ~6x6 nm area, using the same criteria for both datasets. Pairs with distances that differ by more than 10% from 1.36 Å were excluded, which left 136 LDR and 48 HDR atoms. This significant difference already highlights that there is signal degradation in HDR conditions near the thin edge of the sample as can be seen from Fig. 10c. Blurring leads to a change in the apparent dumbbell distance and causes larger fitting errors. In contrast, sharp peaks can still be detected from the edge columns in the LDR dataset. The mean column width, expressed by the standard deviation sigma of a 2D Gaussian, is 68 pm for LDR and 75 pm for HDR. The fitted amplitudes of the double-Gaussian peaks within 2.2 nm distance from the edge are plotted as a histogram in fig. 10d. The most probable phases are by 50-100 mrad larger in LDR compared with HDR. It is remarkable that peaks from thin areas close to the edge of the sample, with phases between 50 and 250 mrad, are absent in the HDR histogram but do exist in the LDR dataset. The most notable difference between the datasets are sharper phase peaks in the LDR reconstruction. In Figure 12e, the peak amplitude divided by its width is plotted as a function of edge distance. While the values for LDR increase nearly linearly with the edge distance, the HDR points are more scattered, and the average sharpness is ~10% lower than for LDR.

Discussion

We demonstrate that atomic resolution imaging and in-line holography realized by focal series reconstruction are feasible at energies between 20 and 300 keV and intensities down to 12 electrons/Å^{2}s. Except for 20 keV, the 1.36 Å resolution benchmark for Si[110] dumbbells has been achieved throughout the explored energy-intensity parameter space. We thus show that neither high voltages nor high intensities are needed for sample analysis with Å and sub-Å resolution. The described new imaging conditions enable aberration-corrected HRTEM to be applied in the rapidly growing research field of hard/soft matter composite materials.

We also find that the measured atomic phase peaks in EWRs of Si[110] wedges always remain smaller than π/2 under both HDR and LDR conditions, which is not expected from theory. This has been observed in similar measurements of wedge-shaped gold samples, while microscope performance improvements seem to reduce this mismatch (Kisielowski at al., 2002). In fact, phase values recovered from exit wave reconstructions that are larger than 1 rad have never before been reported in the literature.

In materials science HRTEM, Debye-Waller (DW) factors are usually introduced to match experiment and simulation. For bulk material, thermal vibrations of each atom are then described by a temperature factor T_N that contains the DW factor B_N. *The latter* is proportional to the mean square displacement $<u_N^2>$:

$$T_N = \exp[-B_N k^2/(4\pi)^2] \qquad \text{with} \qquad B_N = 8/3\, \pi^2 <u_N^2>. \qquad (3)$$

This expression implies deviations from the equilibrium position in three dimensions. However, most of the time only lateral displacements (frozen phonons or DW factors) are considered in electron microscopy, since the 3D object structure is projected into a 2D image plane. Thickness dependent, lateral column displacements on a pm scale that are induced by electron beam irradiation were recently measured in Rh (Specht et al. , 2011), Ge (Alloyeau et al., , 2009), MoS_2 (Kisielowski et al., 2010b) or BN (Alem et al., 2009). An influence of atom displacements in beam direction was measured and explained recently (Alem et al., 2011).

A DW factor of 0.5 $Å^2$ as reported for Si in the literature (Flensburg & Stewart, 1998) does not properly describe the sample-thickness-dependent phase modulation that we observe in our experiments. Adding a mechanical instability term to the usual thermal sample vibrations removes this discrepancy and is consistent with the otherwise unexplained reduction of phase values shown in Fig. 10. It is common practice to include electrical instabilities into the temporal damping function of the CTF, and mechanical instabilities have been treated in a similar manner (Hytch & Stobbs, 1994). A time-dependent displacement of an atom from its equilibrium lattice position can be described by a superposition of phonons of the form

$$\boldsymbol{u}(t) = \boldsymbol{u}_0 \exp[-i\omega(\boldsymbol{k})t]. \quad (2)$$

Here, the dispersion $\omega(\boldsymbol{k})$ and density of phonons depend on material properties. Each phonon carries the energy $\hbar\omega$, which is typically 100 meV or less, so that phonon losses are buried in the width of the zero loss peak (Schroeder & Geiger, 1972) even if monochromated. The field of view of a HRTEM image is expected to contain a high number of longitudinal and transversal phonons. These phonons will traverse the object during the exposure time of typically 0.5 to 1s. If a 1 μm^2 area is exposed under HDR conditions, electrons are delivered at a rate of up to 10^{12} s^{-1}, which is on the order of typical phonon lifetimes (ps to fs). As phonons can travel several hundred nanometers during their lifetime, the phonon density in the field of view will be kept at a high equilibrium level.

The discrepancy between theoretical and experimental EWR phases of silicon evident in our experiments can partly be explained by a "blurring" of atomic scattering potentials by beam-induced lattice vibrations. As observed here, these effects can significantly exceed those of the Debye-Waller for thin samples such as a crystal wedge. Surface phonons should dominate in thin samples and their mean displacement exceeds bulk values by a factor of ~2 (Somorjai & Li, 2010). Surface phonons were first proposed by Rayleigh (1885) and may provide a natural explanation for the observed thickness dependence of the excitation. Also, the presence of phonons beyond an equilibrium density can enhance stochastic diffusion or migration processes. It is remarkable that the particular mechanical instability of 45 pm yields a quantitative signal description for the MTF-corrected experimental exit wave function (Fig. 9f and 9c), and also coincides with the previously measured information limit of TEAM 0.5 (Kisielowski et al., 2008). This points to contribution from partial coherence and microscope stability to the damping factor that we summarize in a vibration.

It should be mentioned that the comparison between simulation and experiment is semi-quantitative in a sense that the actual crystal thickness at the sample edge is not known. However, the curvature of the phase profile envelopes compared in Fig. 9, defined by the maximal peak-to-valley phase and the periodical thickness, is independent of the absolute crystal thickness. Instead, according to the 1S state model this curvature should only depend on the amount of damping by mechanical instabilities if all other parameters are unchanged. The envelope curvature, or the maximal phase, can thus be used to estimate the combined atomic and instrumental vibrations. Possible reasons for the remaining differences between theory and experiment include

1. A gradual change from crystalline Si to amorphous silica at the tip, which gives rise to a defective crystal near the tip. The latter can be described in terms of an additional "static" Debye-Waller factor.
2. increasing contributions of non-linear image components in thicker regions.
3. Noise contribution of thermal diffuse scattering from thicker regions to the image near the tip, due to delocalization at large scattering angles (Forbes et al., 2011).
4. background signal improperly sampled by recording across a limited focal range.

The atomic phase peaks in EWRs of Si[110] are sharper in thicker areas of the wedge sample as compared to the edge, where the thickness corresponds to only a few atoms (Fig. 12). Since simulations predict that the sharpness of phases must decrease with increasing sample thickness (Kisielowski at al., 2001), we conclude that the presence of mechanical instabilities, induced by the electron beam or intrinsic to the microscope, are more significant in thin samples than the expected broadening of the phases with increasing sample thickness. Indeed, a large excitation of flexural phonon modes is predicted in thin regions of a sample (Howie 2004). These can give rise to large thermal displacements of atoms both laterally and in beam direction, which can decrease channeling and lead to a stronger blur of scattering potentials and are consistent with our recent measurrements (e.g. Alloyeau et al., 2009, (Kisielowski et al., 2010b).

Conclusion

It is shown in this paper that current technology can provide atomic resolution transmission electron microscopy across the energy range from 20 to 300 kV. The high brightness electron source and the monochromator that were developed in the context of the TEAM Project (Dahmen et al., 2009) are essential to achieve this goal.

In high resolution TEM for materials science, atomic displacements by knock-on events and plasmon excitations are considered most relevant (Rose, 2009; Egerton et al., 2004). Knock-on damage is relevant above a material-dependent energy threshold and can therefore be avoided by choosing an electron energy below this threshold. As an example, the threshold for single atom displacement from a silicon crystal is 255 keV, and ~86 keV for graphene (Zobelli et al., 2007). Dedicated instruments are being developed that operate at 20 keV, which would eliminate knock-on effects for most materials. However, low-voltage TEM has high demands on the stability of the electron source and optics as well as for aberration correction, as we showed in this work. Aberration correction remains a limiting factor for resolution at 20 keV, which is why this matter is currently addressed worldwide (e.g. Kaiser et al., 2011).

The low-dose rate HRTEM imaging technique described in this paper is a suitable approach to imaging of beam-sensitive samples. It is known in structural biology that inelastic scattering can produce irreversible object damage already at lower energy losses of a few eV. This limits the dose and ultimately the resolution e.g. for a single cryo TEM image. The most relevant beam damage effects for native biological material embedded in vitreous ice are the breaking of chemical bonds by inelastic scattering events and subsequent chemical disintegration of molecules, referred to as ionization damage. It is especially severe for low atomic number elements such as carbon or hydrogen, where the ratio of elastic to inelastic scattering is roughly 1:4 (Henderson 1995). Ionization damage can occur at any electron energy, so that the accumulated electron dose per sample area is usually taken as the decisive parameter. In materials science, ionization damage becomes relevant for imaging “soft” materials such as small organic molecules, where breaking of a small number of chemical bonds can displace an atom. When studying such objects, the total dose has to be kept at a minimum during analysis. This can be achieved under LDR conditions if the total exposure time is controlled.

A direct dose rate dependence for HRTEM has been unexplored to date. However, the increased gun brightness needed to achieve higher resolution has created a situation where beam-induced lattice vibrations can exceed the magnitude of Debye-Waller factors. As a result, the sample integrity can be compromised during the investigations in HDR conditions. Here it is shown that the issue of beam-induced object alterations can be addressed by delivering electrons at a low dose rate at voltages adjustable from 20-300 kV. We find that a reduction of dose rate and accumulated dose is beneficial, as it improves the signal quality while maintaining resolution. The effect is thickness-dependent and documented in figures 10 and 12. Recent experiments with a variety of materials systems including graphene, MoS_2, (Hansen et al., 2011), STO (unpublished), and rhodium on alumina (Specht et al., 2011b) reveal similar improvements of structure stability and signal quality with decreasing dose rates. The effect becomes most obvious in thin films if the number of electrons/$Å^2$s is decreased below 100. Moreover, dose rates as low as $12e^-/Å^2$s in combination with exit wave reconstruction from large data sets allow treating the imaging of soft and hard matter on equal, dose-rate limited footing.

However, it was recently demonstrated for thin Rhodium crystals that a quantification of atom movements is challenging. Beam-induced lattice vibrations can be traded with mechanical microscope stability, unless local displacements in the range of 10-30 pm can be extracted from images of columns containing a few atoms (Specht et al., 2011b). A direct measurement of beam-induced lattice vibrations becomes accessible in TEAM 0.5, which provides an information limit better than 0.5 Å and therefore has extraordinary mechanical stability.

The ability to control voltage and dose rate to a level where only a few electrons are detected in a single image, demonstrated here for the case of Si[110], can be of significant relevance to other materials. Examples of interest include organic molecules attached to crystalline surfaces. We suggest that high resolution electron microscopy can be significantly enhanced by gaining accurate control over accumulated electron dose, dose rate, and energy.

Acknowledgements

Colin Ophus is thanked for help with imaging simulations and for fruitful discussions. Roar Kilaas provided support for the EWR software. Christopher Skelton and Abhay Gautam helped with sample preparation. The investigation of Si samples is part of the Soft Matter program, which is supported by the U.S. Department of Energy under Contract No. DE-AC02-05CH11231. The low voltage tuning of the TEAM 0.5 microscope at the NCEM is supported by the Office of Science, Office of Basic Energy Sciences, Scientific User Facilities Division, of the U.S. Department of Energy under Contract No. DE-AC02—05CH11231. During this work, HAC was hosted by the Lawrence Berkeley National Laboratory, Materials Science Division, in the context of the HELIOS/SERC program. HAC acknowledges IPN (SIP, COFAA) and CONACYPT (grant 129207) for financial support.

Disclaimer

References

Alem, N.,Yazyev, O.V., Kisielowski, C., Denes, P., Dahmen, U., Hartel, P., Haider, M., Bischoff, M., Jiang, B., Louie, S.G. & Zettl, A. (2011). Probing the Out-of-Plane Distortion of Single Point Defects in Atomically Thin Hexagonal Boron Nitride at the Picometer Scale. Phys. Rev. B **106**, 126102.

Alem, Nasim; Erni, Rolf; Kisielowski, Christian; Rossell, Marta D.; Gannett, Will; Zettl, A. Atomically thin hexagonal boron nitride probed by ultrahigh-resolution transmission electron microscopy, (2009) Phys. Rev. B 80, 1554259

Alloyeau, D., Freitag, B., Dag, S., Wang, L.W. & Kisielowski, C. (2009). Atomic-resolution three-dimensional imaging of germanium self-interstitials near a surface: Aberration-corrected transmission electron microscopy. Phys. Rev. B **80**, 014114.

Bammes, B.E., Jakana, J., Schmid, M.F. & Chiu, W. (2010). Radiation damage effects at four specimen temperatures from 4 to 100 K. J. Struct. Biol. **169,** 331-341.

Barton, B., Song C. & Kisielowski, C. (2011). Atomic resolution at 50 – 300 kV obtained using low dose rate HRTEM. Microsc. Microanal. **17**, 1266 - 1267.

Battaglia, M., Contarato, D., Denes, P. & Giubilato, P. (2009). Cluster imaging with a direct detection CMOS pixel sensor in transmission electron microscopy. Nuclear Instruments & Methods In Physics Research A **608,** 363-365.

Dahmen, U., Erni, R., Radmilovic, V., Kisielowski, C., Rossell, M.-D. & Denes, P. (2009). Background, status and future of the Transmission Electron Aberration-corrected Microscope project, Phil. Trans. R. Soc. A **367**, 3795-3808.

Egerton R.F., Li P. & Malac M. (2004). Radiation damage in the TEM and SEM. Micron **35**, 399-409.

Erni, R. (2010). Aberration-corrected Imaging in Transmission Electron Microscopy. Imperial College Press, London

Flensburg, C. & Stewart, R.F. (2008). Lattice dynamical Debye-Waller factor for silicon. Phys. Rev. B **60**, 284-291.

Forbes, B.D., D'Alfonso, A.J., Findlay, S.D., Van Dyck, D., LeBeau, J.M., Stemmer, S. & Allen, L.J. (2011). Thermal diffuse scattering in transmission electron microscopy. Ultramicroscopy **111**, 1670-1680.

Freitag, B., Knippels, G., Kujawa, S., Tiemeijer, P.C., Van der Stam, M., Hubert, D., Kisielowski, C., Denes, P., Minor A. & Dahmen, U. (2008). First performance measurements and application results of a new high brightness Schottky field emitter for HR-S/TEM at 80-300kV acceleration voltage. EMC 1 Instrumentation and Methods, 55–56.

Haider, M., Uhlemann, S., Schwan, E., Rose, H., Kabius, B. & Urban, K. (1998). Electron microscopy image enhanced. Nature **392**, 768-769.

Hansen, L. P., Ramasse, Q. M., Kisielowski, C., Brorson, M., Johnson, E., Topsøe, H. & Helveg, S. (2011). Atomic-Scale Edge Structures on Industrial-Style MoS2 Nanocatalysts. Angew. Chem. Int. Ed. **50**, 10153–10156.

Henderson, R. (1995). The Potential and Limitations of Neutrons, Electrons and X-Rays for Atomic Resolution Microscopy of Unstained Biological Molecules. Q. Rev. Biophys. **28**, 171-193.

Howie, A. (2004). Hunting the Stobbs factor. Ultramicroscopy **98**, 73-79.

Hsieh, W.-K., Chen, F.-R., Kai, J.-J. & Kirkland, A.I. (2004). Resolution extension and exit wave reconstruction in complex HREM. Ultramicroscopy **98**, 99-114.

Hytch, M.J. & Stobbs, W.M. (1994). Quantitative comparison of high resolution TEM images with image simulations. Ultramicroscopy **53**, 63-72.

Kabius, B., Hartel, P., Haider, M., Müller, H., Uhlemann, S., Loebau, U., Zach, J. & Rose, H., (2009). First application of Cc-corrected imaging for high-resolution and energy-filtered TEM. J. Electron Microsc. **58**, 147–155.

Kaiser, U., Biskupek, J., Meyer, J.C., Leschner, J., Lechner, L., Rose, H., Stöger-Pollach, M., Khlobystov, A.N., Hartel, P., Müller, H., Haider, M., Eyhusen, S. & Benner, G. (2011). Transmission electron microscopy at 20 kV for imaging and spectroscopy. Ultramicroscopy **111**, 1239-1246.

Kim, Y.-K. & Rudd, M. E. (1994). Binary-encounter-dipole model for electron-impact ionization. Phys. Rev. A **50**, 3954-3967.

Kisielowski, C., Hetherington, C.J.D., Wang, Y.C., Kilaas, R., O'Keefe, M.A. & Thust, A. (2001). Imaging columns of the light elements C, N, and O with sub-Angstrom resolution, Ultramicroscopy **89**, 243–263.

Kisielowski, C. & Jinschek, J. (2002). On the Feasibility to Investigate Point Defects by Advanced Electron Microscopy. In Physik Mikrostruktuierter Halbleiter 27, Specht, P., Wetherford, T.R., Kiesel, P., Marek, T. & Malzer, S. (Eds.), pp. 137-144. Erlangen-Nuernberg: the University of Erlangen.

Kisielowski, C., Freitag, B.,. Bischoff, M., van Lin, H., Lazar, S., Knippels, G., Tiemeijer, P., van der Stam, M., von Harrach, S., Stekelenburg, M., Haider, M., Muller, H., Hartel, P., Kabius, B., Miller, D., Petrov, I., Olson, E., Donchev, T., Kenik, E.A., Lupini, A., Bentley, J., Pennycook, S., Minor, A. M., Schmid, A. K., Duden, T., Radmilovic, V., Ramasse, Q., Erni, R., Watanabe, M., Stach, E., Denes, P. & Dahmen, U. (2008). Detection of single atoms and buried defects in three dimensions by aberration-corrected electron microscopy with 0.5 Å information limit. Microsc. Microanal. **14**, 454-462.

Kisielowski, C., Specht, P., Alloyeau, D., Erni, R. & Ramasse, Q. (2009). Aberration-corrected electron microscopy imaging for nanoelectronics applications. In *Frontiers of Characterization and Metrology for Nanoelectronics*, Seiler, D.G., Diebold, A.C., McDonald, R., Garner, C.M., Herr, D., Khosla, R.P. & Secula, E.M. (Eds.), pp. 231 – 241. American Institute of Physics Conference Proceedings **1173.**

Kisielowski, C, Specht, P., Barton, B. & Jiang, B. (2010). Improving on phase contrast by harvesting more spatial frequencies at different acceleration voltages. In *Proceedings of the 17th International Microscopy Congress*, Brazil 2010.

Kisielowski, C., Ramasse, Q., Hansen, L.P., Brorson, M., Carlsson, A., Molenbroek, A.M., Topsoe, H. & Helveg, S. (2010). Imaging MoS_2 Nanocatalysts with Single-Atom Sensitivity. Angew. Chem. Int. Ed. **49**, 2708-2710.

Lentzen, M. (2004). The tuning of a Zernike phase plate with defocus and variable spherical aberration and its use in HRTEM imaging. Ultramicroscopy **99**, 211-220.

Medalia, O., Weber, I., Frangakis, A. S., Nicastro, D., Gerisch, G. & Baumeister, W. (2002). Macromolecular architecture in eukaryotic cells visualized by cryoelectron tomography. Science **298**, 1209-1213.

Müller, H. (2012). Personal communication.

O'Keefe, M.A., Hetherington, C.J.D., Wang, Y.C., Nelson, E.C., Turner, J.H., Kisielowski, C., Malm, J.-O., Mueller, R., Ringnalda, J., Pan, M. & Thust, A. (2001). Sub-Ångström high-resolution transmission electron microscopy at 300keV. Ultramicroscopy **89**, 215-241.

Rose, H. (2009). Future trends in aberration-corrected electron microscopy. Phil. Trans. R. Soc. A **367**, 3809–3823.

Sawada, H., Hosokava, F., Sasaki, T., Yuasa, S., Kawazoe, M., Terao, M., Kaneyama, T., Kondo, Y., Kimoto, K. & Suenaga, K. (2010). Chromatic Aberration Correction by Combination Concave Lens. Microsc. Microanal. **16**, 116-117.

Schroeder, B. & Geiger, J. (1972). Electron-spectrometric study of amorphous germanium and silicon in the two-phonon region. Phys. Rev. Lett. **28**, 301-303.

Somorjai, G.A. & Li, Y. (2010). *Introduction to surface chemistry and catalysis*. New Jersey: Wiley and Sons.

Specht, P., Gulotty, R.J., Barton, D., Cieslinski, R., Rozeveld, S., Kang, J.H., Dubon, O.D. & Kisielowski, C. (2011). Quantitative Contrast Evaluation of an Industry‐Style Rhodium Nanocatalyst with Single Atom Sensitivity. ChemCatChem **3**, 1034-1037.

Specht, P., Barton, D., Kang, J., Cieslinski, R., Dubon, O. & Kisielowski, C. (2011). Direct Imaging of Rhodium Crystal Surface Structures with Signal Recovery by Low Dose Microscopy. Microsc. Microanal. **17** Suppl. 2, 1064-1065.

Tiemeijer, P.C., Bischoff, M., Freitag, B. & Kisielowski, C. (2008). Using a monochromator to improve the resolution in focal-series reconstructed TEM down to 0.5ÅM. In *EMC 1 Instrumentation and Methods*, Luysberg, M., Tillmann, K. & Weirich, T. (Eds.), pp. 53–54.

Tiemeijer, P.C., Bischoff, M., Freitag, B. & Kisielowski, C. Using a monochromator to improve the resolution in TEM to below 0.5 A. Part I: Creating highly coherent monochromated illumination, Ultramicroscopy (2012), doi:10.1016/j.ultramic. 2012.01.008

Van Aert, S., Geuens, P., Van Dyck, D., Kisielowski, C. & Jinschek, J. R. (2007). Electron channelling based crystallography. Ultramicroscopy **107**, 551-558.

Zobelli, A., Gloter, A., Ewels, C., Seifert, G. & Colliex, C. (2007). Electron knock-on cross section of carbon and boron nitride nanotubes. Phys. Rev. B **75**, 245402.

Figures

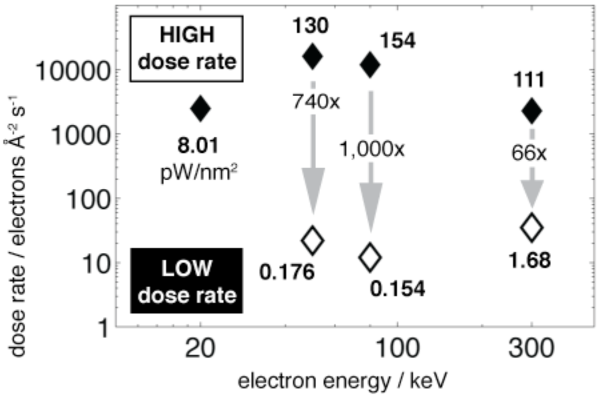

Figure 1. *Electron dose rate (beam intensity) and energy were used as tunable parameters to study the effect of beam-sample interactions. While the high dose rate (HDR) conditions (black diamonds) used in our experiments are typical for imaging of hard materials with a high brightness gun (XFEG), HRTEM imaging under low dose rate (LDR) conditions (white) is demonstrated in this paper. Numbers printed in bold give the corresponding beam power for each experiment in pW/nm^2, and the dose rate reduction is given for pairs of HDR/LDR conditions. A resolution of better than 1.36 Å was achieved for all data points except at 20 keV, where the information limit is estimated at ~1.8 Å. For details see text.*

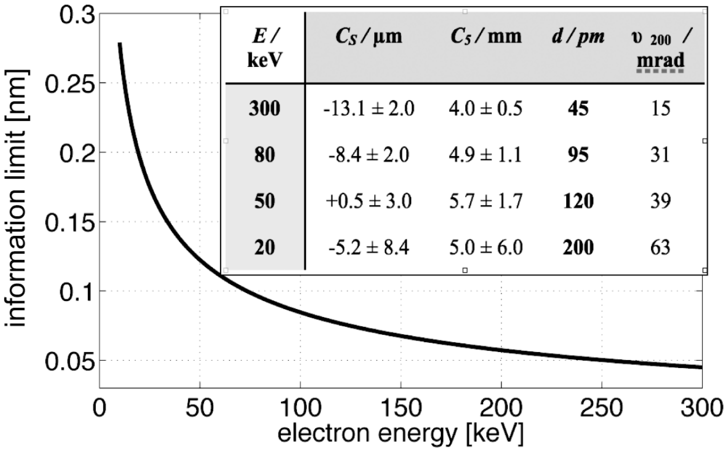

E / keV	**C_S / µm**	**C_5 / mm**	**d / pm**	**υ_{200} / mrad**
300	-13.1 ± 2.0	4.0 ± 0.5	**45**	15
80	-8.4 ± 2.0	4.9 ± 1.1	**95**	31
50	+0.5 ± 3.0	5.7 ± 1.7	**120**	39
20	-5.2 ± 8.4	5.0 ± 6.0	**200**	63

Figure 2. *Spherical aberration coefficients $C_S = C_3$ and C_5, Bragg angle υ_{200} for the [200] dumbbell periodicity, and estimated information limit d of the TEAM 0.5 for electron energies used in this work. For the measured information limit of the instrument of 45 pm at 300 keV, a maximal scattering angle of 44 mrad can be derived that is correctly transferred to an image point by the optics. This angle was used to estimate the information limit. Energies above 50 keV permit resolution of 1.36 Å Si[110] dumbbells, as confirmed by our experiments. At 20 keV, the information limit is expected around 2.0 Å (cf. Fig. 4). We assume a voltage-independent chromatic aberration coefficient (C_C) of 1.2 mm (Kisielowski et al., 2001). Simulated voltage-dependent C_C values reach from 0.8 mm at 20 kV to 2.1 mm at 300 kV (see text).*

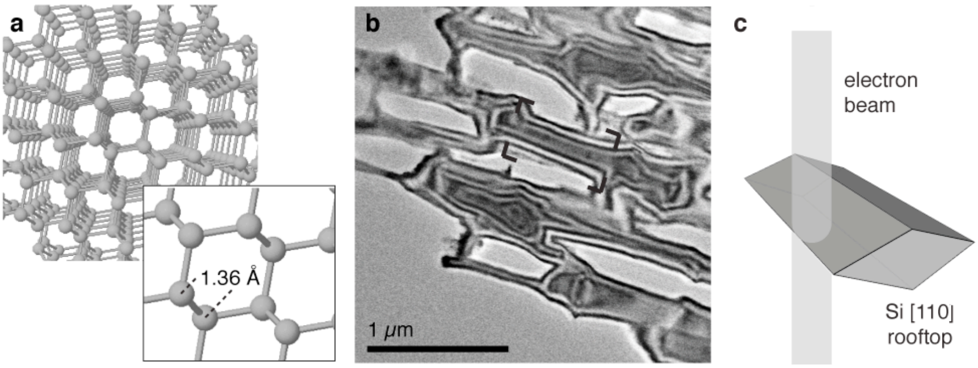

Figure 3. a: *Model of a Si crystal viewed along [110] direction. The characteristic dumbbells have a projected distance of 1.36 Å.* ***b:*** *Low magnification TEM image of the edge of a Si[110] sample, recorded with large underfocus at 80 keV. The sample was prepared from a wafer by dimpling and subsequent etching with hydrofluoric acid and potassium hydroxide (see text).* ***c:*** *The etching process produces a "rooftop" topography, which yields a sample with plane faces and a thickness at the edge of only a few atomic layers.*

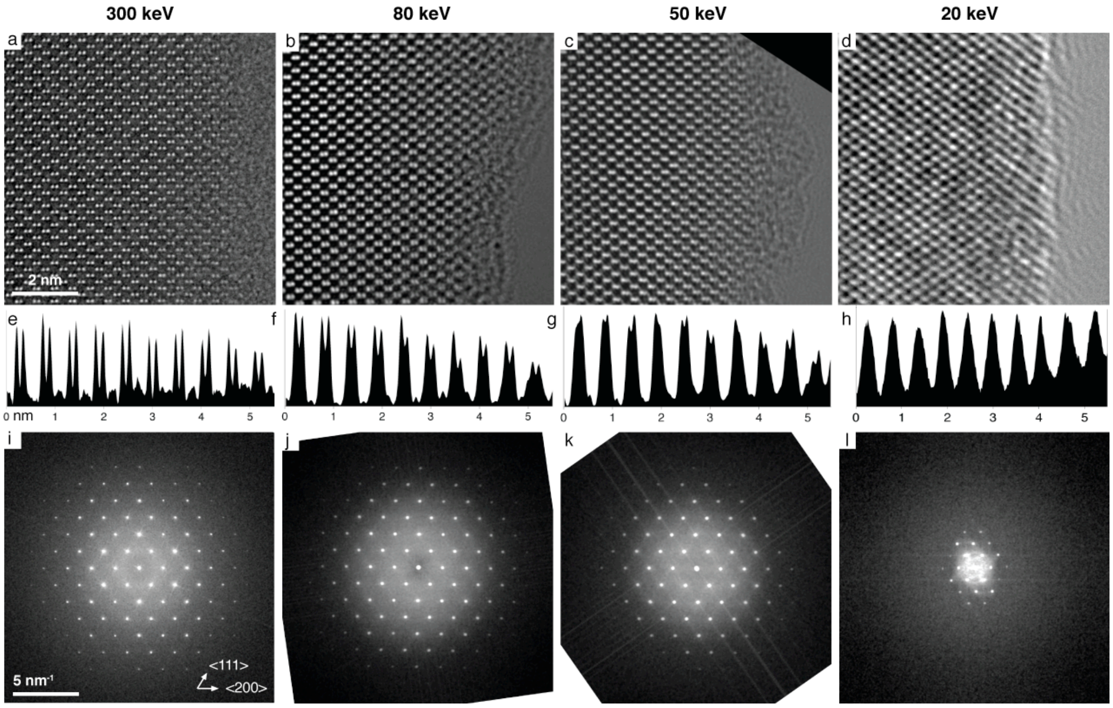

Figure 4. ***a-d:*** *Edge of Si[110] wedge imaged with the TEAM 0.5 at 300, 80, 50 and 20 kV at a primary magnification of 330,000. The overfocus values are (55 ± 11) Å for 20 kV, (88 ± 11) Å for 50 kV, (77 ± 11) Å for 80 kV and (60 ± 20) Å for 300 kV.* ***e-h:*** *Line plots of image intensities corresponding to (a-d) in [100] direction. The characteristic 1.36 Å dumbbells can be resolved at 300, 80 and 50 keV, as indicated by the dips in the intensity peaks. Dumbbell resolution is not present in image in the 20 keV image (d,e) due to the presence of residual aberrations. The contrast delocalization at 20 kV observed at the sample edge is a direct consequence of the increased scattering angles and wave aberration (cf. Fig. 2).* ***i-l:*** *This can be seen in the image power spectra: while at 300, 80 and 50 kV structure factors up to [800] (1/0.68 Å) are present, the transfer at 20 keV is limited to the <400> lattice vector (1/1.36 Å). The presence of reciprocal lattice vectors does not directly reflect image resolution, due to dynamic scattering in the crystal.*

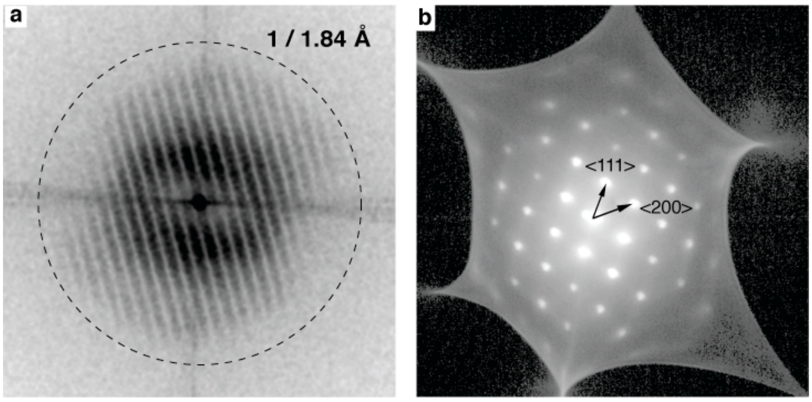

Figure 5. *Residual aberrations are a limiting factor for imaging at 20 keV.* ***a:*** *Young's fringes in the power spectrum of ultra-thin amorphous carbon film indicate a linear information limit of ~1.8 Å. This resolution is slightly higher then estimated (cf. Fig. 2; see text).* ***b:*** *Diffraction pattern of a Si[110] rooftop sample at 20 keV.*

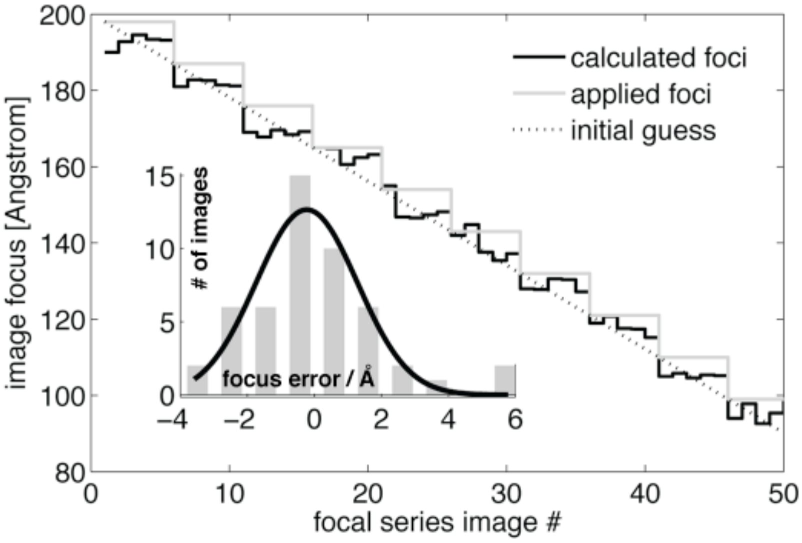

***Figure 6**. A stepped focal series is used to test the focal stability in the TEAM 0.5 and the measurement precision of the program MacTempas at 80 kV. The focus was decreased in steps of 11 Å every 5 images (gray curve). As an initial guess, a linear decrease by 2.2 Å per image was used (dotted line). The values calculated as a result of the exit wave reconstruction (black curve) follow the step shape of the instrumental foci, with a mean offset of -5 Å. The inset shows a histogram of the deviation of the measured foci from a perfect step function. The standard deviation of the Gaussian fit (black curve) is only 2.1 Å.*

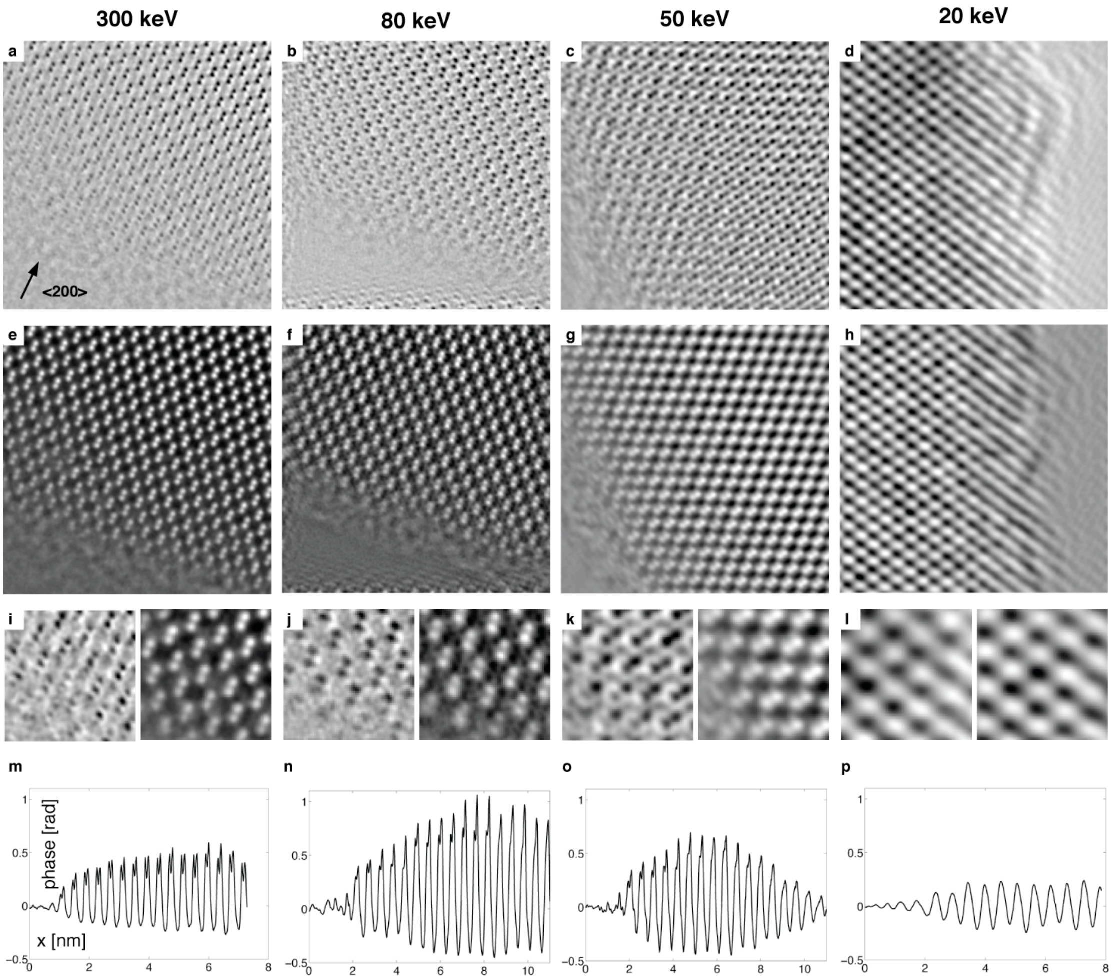

***Figure** 7. Focal series reconstruction of Si[110] rooftop edges (cf. Fig. 3c) performed at 300, 80, 50 and 20 kV. **a-h:** Amplitudes and phase of the reconstructed wave in a plane containing the wedge tip are shown for a 5.8 x 5.8 nm area. The wedge is terminated by a ~2 nm thick amorphous oxide layer. The <200> dumbbell direction is indicated (arrow in (a)). **i-l:** The magnified areas of 1.5 nm side length show that the 1.36 Å dumbbells can be resolved in phase and amplitude at 300, 80 and 50 keV. At 20 keV, this resolution is not permitted due to the presence of residual wave aberrations (cf. Figs. 4,5). **m-p:** Phase profiles along a three pixel-wide line in <200> direction.*

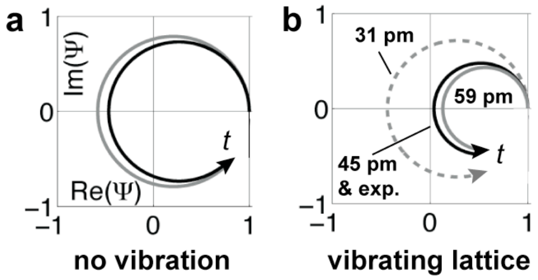

Figure 8**: Complex representation (Argand plot) of the reconstructed exit wave function of a Si[110] wedge, as predicted by the 1S state model.* ***a: *Argand plot of the simulated EW (gray) and a reconstruction from a focal series of 40 images (black, cf. Fig. 9). Without lattice vibrations, the diameter $|2\ c_{00}\ \psi_{00}|$ of the circle is >1, so that the phase reaches π at half the periodical thickness. However, such large values were never observed in experiments.* ***b:*** *Reconstructions from focal series simulated including combined microscope and beam-induced sample vibrations of 31, 45 and 59 pm standard deviation, included into a damping function. While phase wrapping still occurs with only 31 pm of vibration, phases are always <π/2 if a total vibration of ≥45 pm is present, which approximates the information limit of TEAM 0.5. Atomic phases reach a maximum before falling off to zero at half the periodical thickness, as observed in the experiments. A vibration by 45 pm matches best the experimental values (exp.). All simulations were done using parameters for the TEAM 0.5 at 80 keV, and a mean atomic Debye-Waller factor of 0.5 Å^2. In (a), the circle diameter is estimated from the modulus of atom columns with phase π/2. In (b), the diameter was calculated from the largest observed phases.*

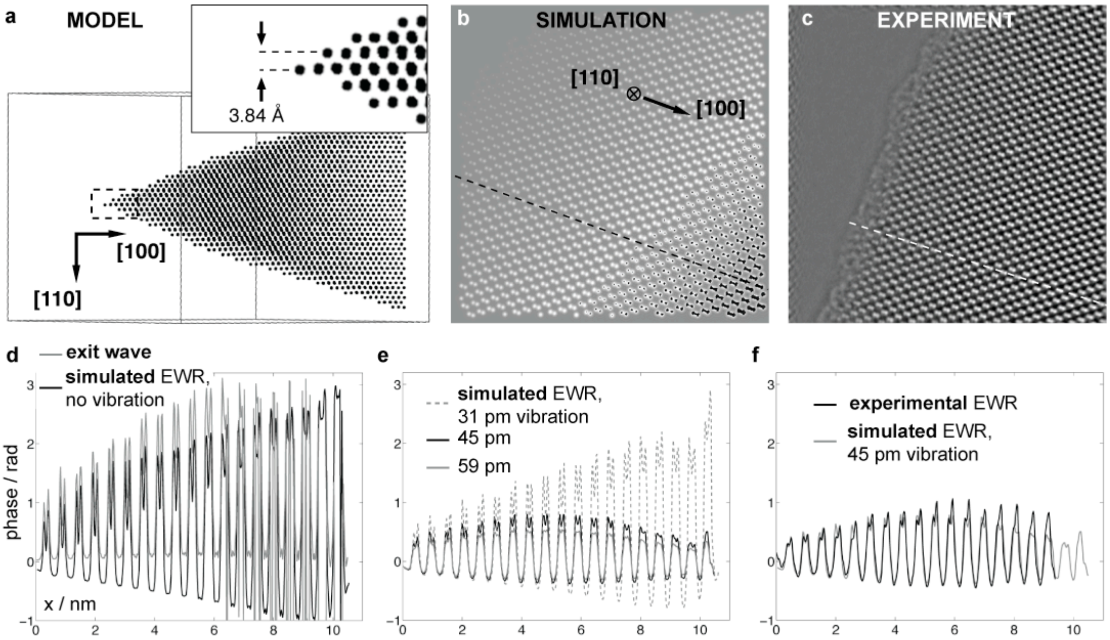

Figure 9**. Comparison of an experimental focal series reconstruction of a Si[110] wedge with multi-slice simulations for the TEAM 0.5 at 80 keV.* ***a: *The Si wedge model used for simulation seen from [111] direction, perpendicular to the beam axis [110]. It has single atoms at the edge and is 44 planes thick at the base, with a wedge angle of ~40°. Inset: view of the wedge tip.* ***b-c:*** *Exit wave phases in a 11.8 x 11.8 nm area at the edge.* ***b:*** *Multi-slice simulation. The lattice is not aligned with the image pixels to avoid artifacts.* ***c:*** *Experimental reconstruction from a focal series recorded under HDR conditions, corrected for the camera MTF.* ***d-f:*** *Phase profiles along the dashed lines in (b) and (c).* ***d:*** *The original EW shows phase wrapping at half periodical thickness, as expected from theory (cf. Fig. 8). If the EW is reconstructed from a focal series without atomic vibrations, equivalent peak-to-valley phases are obtained. The offset of the minima is caused by the absence of low spatial frequencies in the image series.* ***e:*** *Simulated EWRs assuming lattice vibrations with 59, 45 and 31 pm mean atomic displacement (cf. Fig. 8). At 31 pm vibration, the blurring of*

Coulomb potentials is small enough to reach a phase of π. For ≥ 45 pm, the column phases peak before falling off to nearly zero at half the periodical thickness. ***f:*** *The same phase modulation is observed for the experimental EWs. The phase profile (black) shows a good match to the simulation for 45 pm, which is shown for comparison (grey). All EWRs were calculated from 40 images, using the same primary foci between +33 and -11 nm, C_S = -8.43 µm and C_5 = 5.5 mm.*

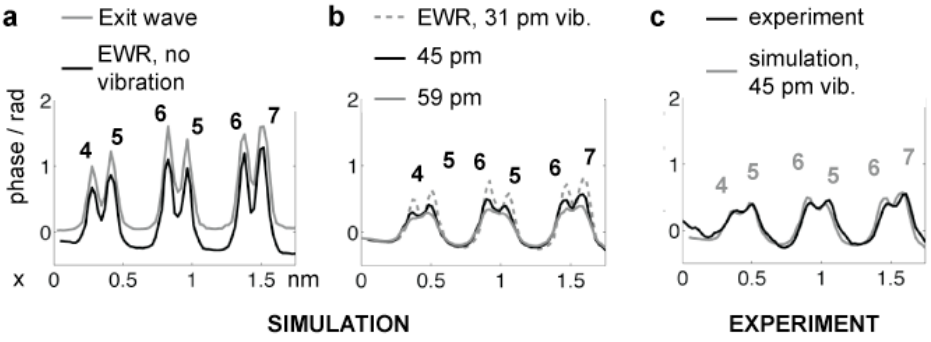

Figure 10. *Phase profiles from EWs of a Si[110] wedge tip (cf. Fig. 9a) with column thicknesses from 4 to 7 atoms. We used experimental and simulation parameters as described in Fig. 9.* ***a:*** *Without lattice vibrations, the true phase is almost perfectly reconstructed from a focal series of 40 images recorded with the TEAM 0.5 at 80 keV.* ***b:*** *When lattice vibrations are taken into account, the phase sensitivity is reduced by 60-70%, which makes counting of atoms along a column difficult in the presence of noise. For a vibration by 59 pm, dumbbell resolution is nearly lost.* ***c:*** *A vibration by 45 pm describes well the experiment (black curve). Atom numbers in (c) refer to the simulation (gray curve), as they are unknown for the experiment.*

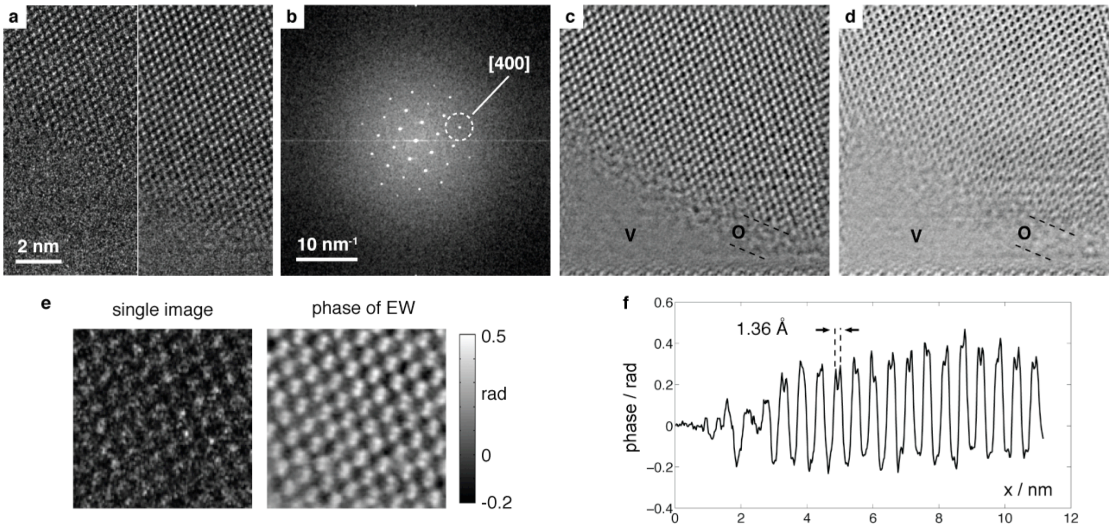

Figure 11. *Low dose rate exit wave reconstruction of a Si[110] wedge from images recorded with 12* $e^-/\text{Å}^2s$ *at 80 keV.* ***a:*** *Left half: single image from focal series, right half: average of 5 LDR images recorded at the same focus.* ***b:*** *Power spectrum of a single image, showing structure factors to a resolution better than 1.36 Å ([400] reflection).* ***c,d:*** *Phase and amplitude of the exit wave reconstructed using 27 averages, with defoci ranging from +33.0 to +4.4 nm (O: oxide layer, V: vacuum).* ***e:*** *Single image and reconstructed phase for a 2.3 x 2.3 nm area. While atomic columns can hardly be recognized in the noisy image, The dumbbells are clearly resolved in the EW phase.* ***f:*** *Line plot of the phase in <200> direction. The dips show 1.36 Å resolution.*

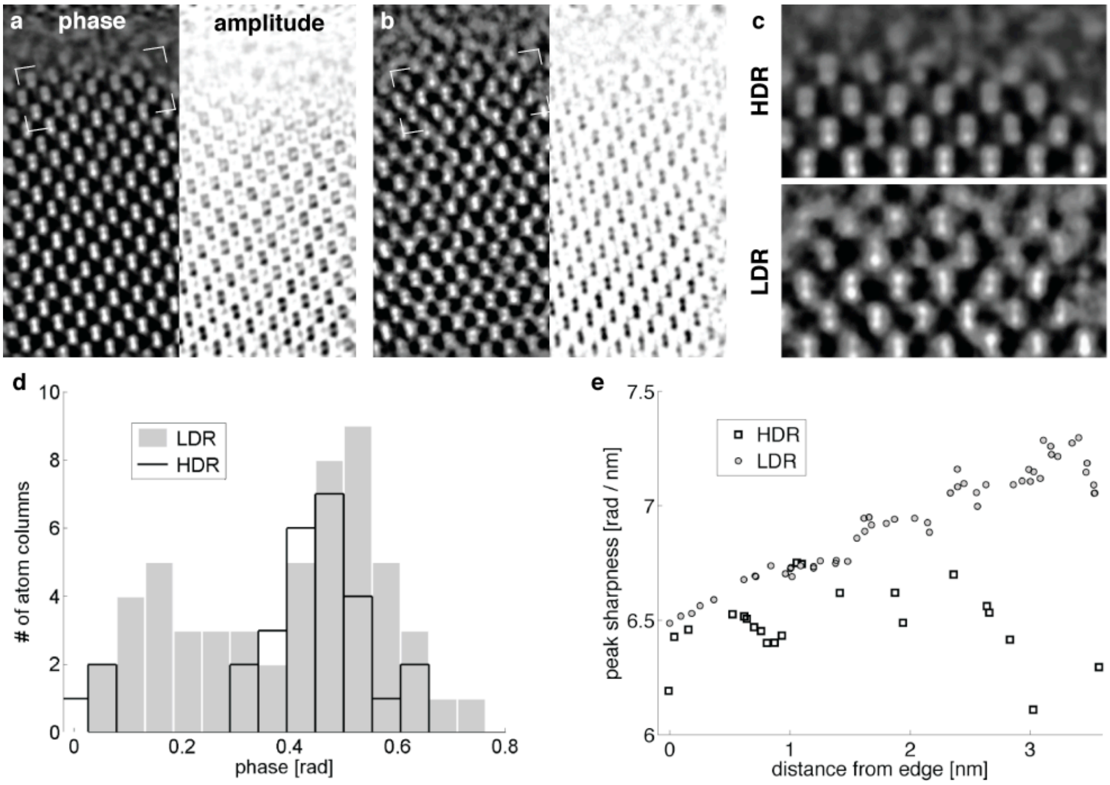

Figure 12**. The effect of low dose rate imaging on exit wave reconstruction.* ***a,b: *Phase (left half) and modulus (right half) of EWs from HDR (a, 12,000 $e^-/\AA^2s$) and LDR data (b, 56 $e^-/\AA^2s$).* ***c:*** *Comparison of the boxed areas in (a) and (b) showing the phase of columns at the crystal edge.* ***d:*** *Histogram of phase peak amplitudes within a 2.2 nm from the crystal edge.* ***e:*** *The peak sharpness (fitted peak amplitude / sigma) for HDR and LDR plotted as a function of distance from the edge.*

Tables

E / keV	φ_{max} / rad	t_{max} / nm	D_{00} / nm
20	0.47	6.2 ± 2.0	11.0 (12.5)
50	1.1	5.2 ± 1.0	17.5 (19.5)
80	1.3	8.0 ± 1.0	20.5 (22.0)
300	0.75	6.2 ± 1.0	29.0 (32.5)

Table 1: *Maximal experimental phase peaks φ_{max}, occuring at a crystal thickness t_{max}, and calculated periodical thicknesses D_{00} for different electron energies and a Debye-Waller factor of 0.5 $Å^2$. (Values in brackets: D.-W. factor of 2.0 $Å^2$). The t_{max} were estimated from the data shown in Fig. 7 m-p, assuming a perfect 50^o Si[110] wedge which is four atoms thick at its tip.*

Supplementary Figures

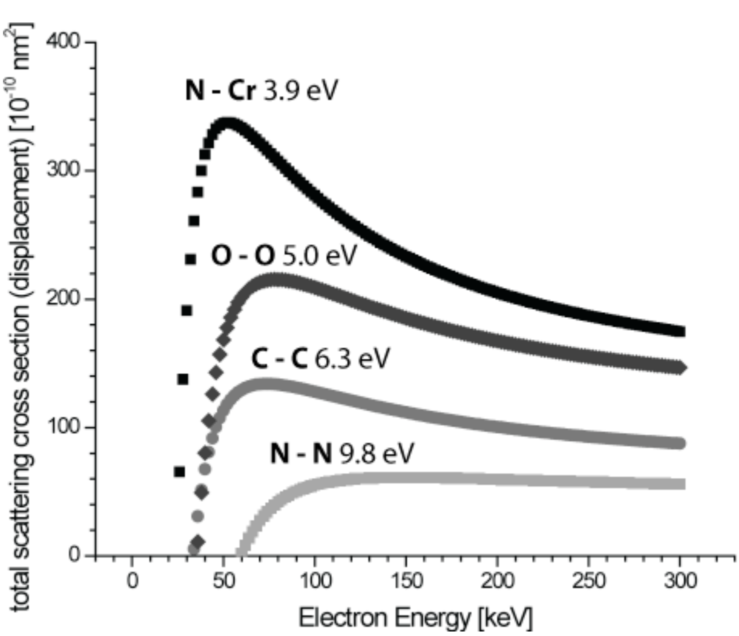

Supplementary Figure 1: *Calculated cross-sections for displacement (knock-on) damage events for selected diatomic molecules composed of light elements. The binding energies are given for each molecule.*

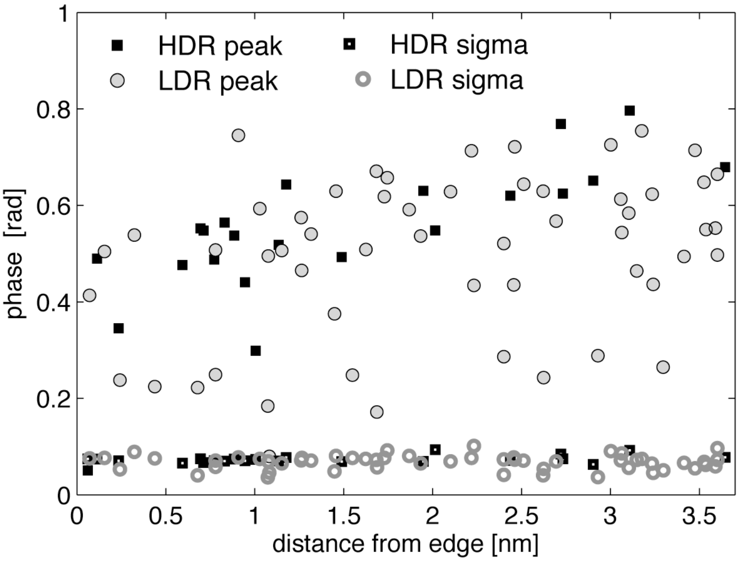

Supplementary Figure 2: *Amplitudes (peak) and standard deviations (sigma) of a fit of double Gaussians to dumbbells in the EWR phase of a Si[110] at 80 kV (cf. Fig. 12), plotted as a function of distance from the edge. Black: high dose rate conditions, gray: low dose rate conditions.*